Soft Matter

Accepted Manuscript

ROYAL SOCIETY OF CHEMISTRY

www.rsc.org/softmatter

ARTICLE TYPE www. rsc.org/xxxxxx | XXXXXXXX

Directed Self-assembly of Cylinder-forming Diblock Copolymers on Sparse Chemical Patterns

Yong-Biao Yang,[a†] Young Joo Choi,[b] Sang Ouk Kim[b] and Jaeup U. Kim[*a]

Received Xth XXXXXXXXXX 20XX, Accepted Xth XXXXXXXXX 20XX
First published on the web Xth XXXXXXXXXX 200X
DOI: 10.1039/b000000x

Using both theory and experiment, we investigate the possibility of creating perfectly ordered block copolymer nanostructures on sparsely patterned substrates. Our study focuses on scrutinizing the proper pattern conditions to avoid undesired morphologies or defects when depositing cylinder-forming AB diblock copolymer thin films on the substrates which are mostly neutral with periodic stripe regions preferring the minority domain. By systematically exploring the parameter space with self-consistent field theory (SCFT), the optimal conditions for target phases are determined, and the effects of the chemical pattern period and the block copolymer film thickness on the target phase stability are also studied. Furthermore, as a sample experimental system, almost perfectly aligned polystyrene-*block*-poly(methyl methacrylate) (PS-*b*-PMMA) diblock copolymers are demonstrated. After pattern transfer process, highly-ordered Al nonodot arrays following the initial vertically aligned cylinder pattern are created. This systematic study demonstrates the ability to control the structure and position of nanopatterns on sparse chemical pattern.

1 Introduction

Nanomaterials with patterned surface of versatile functionality are potentially useful in many high-tech fields such as lithography, magnetic data storage, microelectronic devices and photonic crystals.[1–11] Motivated by the rapidly growing industrial requirement, the innovation of nano-fabrication technique has attracted tremendous attention during the past decades, and the ongoing challenges include changing the nanopattern period to even smaller or larger dimensions, creating special pattern shapes such as square arrays, enhancing the long-range order of microdomains, and so on.[8,12–16] Block copolymers (BCPs) are very promising candidates for the fabrication of nanomaterials with such properties, because they have the capability of spontaneously creating various shapes of ordered microdomains including spheres, cylinders, lamellae and bicontinuous networks.[17] In order to fulfill the demand of material property and device functionality, numerous methods have been developed to control the orientation and lateral ordering of microdomains in BCP nanomaterials, such as the use of external fields,[18,19] shear,[20] thermal annealing,[21] solvent annealing,[22] solvent fields[23,24] and patterned substrates.[7,12,25–50] Among these approaches, the directed self-assembly (DSA) of BCPs on patterned substrates is an example of top-down/bottom-up hybrid method. It combines the advantage of thermodynamic self-assembly of BCPs and precise control of lithographic method, providing a potential route to upgrade the nanomaterial fabrication process.

In the process of DSA, templates with properly prepared topographic or chemical prepatterns are usually required. For the former one, *i.e.* graphoeitaxy,[25–33] the alignment of spherical, cylindrical or lamellar microdomains are guided by topographical prepatterns such as grooves or posts. These topographical prepatterns usually have a repeating structure whose period is a few times larger than the natural period of BCPs, and thereby increase the pattern resolution by subdividing the topographical pattern. As for the chemical epitaxy,[34–42] self-assembly of BCPs is guided by chemical prepatterns with strong affinity to certain blocks of BCP chains, and thus final morphologies with good registration to the underlying chemical patterns can be obtained. For nanomaterials requiring ultrahigh-density patterns with high-quality, however, DSA approaches mentioned above are hard to meet such demands.[43] For instance, the pattern density created via chemical epitaxy strongly depends on the template resolution. Because the template is usually prepared by lithographic techniques, the intrinsic resolution of the lithographic method limits the pattern density. As for the graphoeitaxy, although it can enhance the pattern density by subdividing the topographical features, the topographical patterns themselves (groove or post) hinder the improvement of the long-range order of target nanostructures: nanowalls which form grooves occupy a significant fraction of the substrate area, and posts sometimes

[a] *Department of Physics, School of Natural Science, Ulsan National Institute of Science and Technology (UNIST), Ulsan 689-798, Republic of Korea.*
[b] *Department of Materials Science and Engineering, Korea Advanced Institute of Science and Technology (KAIST), Daejeon 305-701, Republic of Korea.*
[†] *Current address: Eduard-Zintl-Institut für Anorganische und Physikalische Chemie and Center of Smart Interfaces, Technische Universität Darmstadt, Alarich-Weiss-Strasse 4, 64287 Darmstadt, Germany.*
[*] To whom correspondence should be addressed. E-mail: jukim@unist.ac.kr

must be treated by special processes to ensure that they do not behave like undesired defects.

The recently introduced density multiplication technology using sparse chemical patterns avoid such problems and can be regarded as an important improvement of DSA.[43–50] This approach turned out to be successful in promoting long-rang order of BCP films while enhancing their pattern density. Its basic idea is to guide the self-assembly by the chemical prepattern of the substrate whose period is usually a few times as large as the natural period of BCPs. The chemical prepattern makes this method essentially a chemical epitaxy. However, at the same time, those microdomains formed on each chemically homogeneous region behave like topographical patterns made by BCP blocks themselves. Through this mechanism, the nanopatterns are enhanced in that the frequency can be doubled, tripled or quadrupled while not reducing the effective surface area, and higher factor of pattern multiplications are in principle possible.[43–46,48] Therefore, this approach offers the potential to increase feature density with relatively small effort and time for the creation of large area nanopatterns.

For the actual realization of this density multiplication method, intensive experimental studies have been performed using substrates with striped patterns,[43,44] hexagonal patterns[45,46] and complex geometries.[47] In one specific work which motivated us, Park *et al.*[44] synergistically combined conventional 193 nm ArF projection photolithography with BCP self-assembly. In their work, highly ordered crossed-cylinder morphologies were generated on striped chemical pattern, and the density of sparse chemical pattern was enhanced by a scale factor of two or three. As a result, they successfuly produced structures with sub-20 nm scale via a single exposure step. Xu *et al.*[47] suggested a method to direct the self-assembly of BCPs within complex two dimentional geometry by using chemical patterns. In their work, the pattern boundaries were used as templates to direct the order of the BCP domains and they also had the role of improving the spatial uniformity of nanopatterns. These results experimentally demonstrated that chemical patterns are as effective as topographical patterns for templating BCP microdomains in thin films, with the purpose of creating well-packed microdomain arrays with long-range order.

On the other hand, for DSA of BCPs, considering the high-dimensional parameter space which imposes diffuiculty for experimentalists to explore for the best condition for defect-less nanostructure formation, theory and simulation[48–50] are often used to reduce time and cost by providing predictions for the resulting morphology. For instance, combining self-consistent field theory (SCFT) and dissipative particle dynamics simulation, Kriksin *et al.*[48] studied the thin films of cylinder-forming block copolymers deposited on various substrates including sparse hexagonal, rectangular and triangle patterns. Their simulations demonstrated that a stable hexagonal morphology in bulk case can be directed with remarkable precision into perpendicular direction using proper nanoscale substrate patterns. It was also shown that the surface control over the ordering and orientation of the hexagonal phase was regulated by the degree of commensurability between polymers and substrate patterning as well by the affinity between the minority domains and the pattern. Yang *et al.*,[42] including two authors of this report, examined thin film nanostructures of cylinder-forming AB diblock copolymers on a chemically patterned substrate with a developed SCFT scheme. By systematically varying the pattern period and film thickness, proper conditions for crossed-cylinder geometry were scrutinized and it was shown that maintaining the film thin enough is a key factor for the stability of the crossed-cylinder phase. These results provided a good explanation for the experiments of ref. 40 exhibiting defects in Figure 2(d) therein. However, possibility of density multiplication was not considered in Yang *et al.*'s simulations.[42] In this report, to proceed further, we report a systematic investigation of the complex nanostructures of cylinder-forming diblock copolymer films deposited on substrates with sparse chemical stripe patterns. For the theoretical part, we perform SCFT calculation,[51,52] which is one of the most accurate theoretical tools that provide quantitative mean field solution for the block copolymer morphology. We scrutinize the proper conditions for fabricating thin films with microdomains of vertical cylinder arrays, and the roles of chemical pattern period and film thickness are also investigated by comparing the free energies between various competing phases. In addition, experimental results are also presented as an example of our simulations.

The outline of this paper is as follows. A brief introduction of diblock copolymer SCFT with substrate interaction is given in section II. In section III, we compare the competing candidate phases to scrutinize the proper physical parameters with which desired morphologies are stable and defects can be removed. In section IV, experimental results using polystyrene-*block*-poly(methyl methacrylate) (PS-*b*-PMMA) diblock copolymers are presented. Finally, we conclude in section V with a brief discussion.

2 Theory and Method

The SCFT formalism and the numerical algorithms used in this report are mostly introduced in ref. 42, so we describe it only briefly here. Our model system consists of AB diblock copolymers, and the total number of copolymer chains is n_p. Each diblock copolymer is composed of an A-block of N_A segments joined to a B-block of N_B segments, giving a total polymerization $N \equiv N_A + N_B$ with A fraction $f \equiv N_A/N$. We assume equal statistical length a and volume ρ_0^{-1} for the two types of segments, so that the total volume of the model system is $V = n_p N/\rho_0$. Using the standard SCFT method,[51–55]

the interaction between A and B segments is described by the usual Flory-Huggins χ parameter, and each copolymer is treated as a Gaussian chain with a natural end-to-end length $R_0 = aN^{1/2}$.

As before, $w_A(\mathbf{r})$ and $w_B(\mathbf{r})$, the fields acting on A and B types of segments at spatial position $\mathbf{r} \equiv (x,y,z)$, is determined by the density of each segment at the same position, $\phi_A(\mathbf{r})$ and $\phi_B(\mathbf{r})$, respectively, as follows:

$$w_A(\mathbf{r}) = \chi N \phi_B(\mathbf{r}) + \xi(\mathbf{r}) - 2\eta_A(x,y)\,\delta(z) aN^{1/2}, \quad (1)$$

$$w_B(\mathbf{r}) = \chi N \phi_A(\mathbf{r}) + \xi(\mathbf{r}) - 2\eta_B(x,y)\,\delta(z) aN^{1/2}. \quad (2)$$

Here $\xi(\mathbf{r})$ is the pressure field that enforces incompressibility condition, $\phi_A(\mathbf{r}) + \phi_B(\mathbf{r}) = 1$, and the terms with delta functions impose the surface interaction energy between the segments and substrate at $z = 0$. Because the substrate is patterned, the interaction terms may have x and y dependence, and thus we introduce a function $\eta_i(x,y)$(i=A or B) which represents the interaction strength between the selective part of the patterned substrate surface and i segment type with the notation that $\eta_i > 0$ means the interaction is attractive.[32,55] Since only two types of segments are involved in this work, $\eta_A - \eta_B$ is the only physically meaningful parameter, and we set $\eta_B = 0$ for convenience. On the other hand, the top surface is assumed to be neutral to the polymers, because it is the ideal condition for the vertical domain alignment we wish to achieve in this work.

Equations (1) and (2) are self-consistently related to the dimensionless A and B segment concentrations,

$$\phi_A(\mathbf{r}) = \frac{V}{Q}\int_0^f ds q(\mathbf{r},s) q^\dagger(\mathbf{r},s), \quad (3)$$

$$\phi_B(\mathbf{r}) = \frac{V}{Q}\int_f^1 ds q(\mathbf{r},s) q^\dagger(\mathbf{r},s), \quad (4)$$

respectively, where the total partition function Q is evaluated as

$$Q = \int d\mathbf{r} q(\mathbf{r},s) q^\dagger(\mathbf{r},s), \quad (5)$$

and the partial partition functions, $q(\mathbf{r},s)$ and $q^\dagger(\mathbf{r},s)$, satisfy the modified diffusion equations

$$\frac{\partial}{\partial s} q(\mathbf{r},s) = \left[\frac{a^2 N}{6}\nabla^2 - w(\mathbf{r})\right] q(\mathbf{r},s), \quad (6)$$

$$-\frac{\partial}{\partial s} q^\dagger(\mathbf{r},s) = \left[\frac{a^2 N}{6}\nabla^2 - w(\mathbf{r})\right] q^\dagger(\mathbf{r},s), \quad (7)$$

respectively. Here $w(\mathbf{r})$ switches from w_A to w_B at the AB junction point, $s = f$. Equation (6) is integrated from $s = 0$ to $s = 1$ with an initial condition, $q(\mathbf{r},0) = 1$, while equation (7) is integrated from $s = 1$ to $s = 0$ with an initial condition, $q^\dagger(\mathbf{r},1) = 1$.

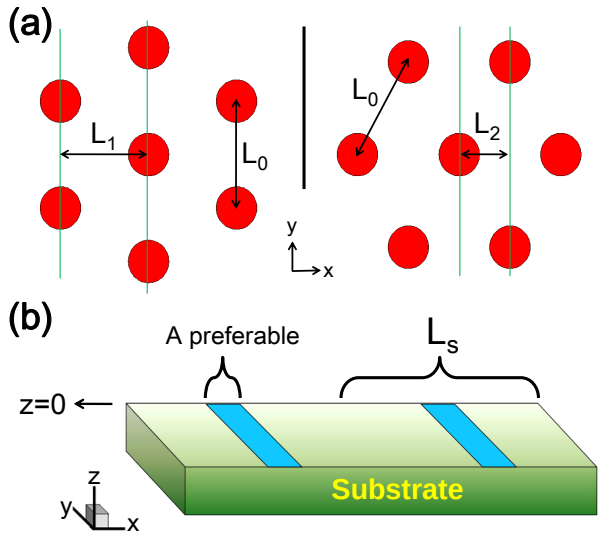

Fig. 1 (a) Schematic illustration of the center-to-center distance $L_0 = 1.69aN^{1/2}$ between adjacent cylinders in bulk phase of AB diblock copolymers ($\chi N = 20$ and $f = 0.3$), and the two types of spacings between cylinder layers, $L_1 = \sqrt{3}L_0/2 = 1.46aN^{1/2}$ and $L_2 = L_0/2 = 0.85aN^{1/2}$; (b) Geometry of a substrate with chemically patterned stripes periodic in x direction. Each A-preferable stripe covers 15% of one period, L_s (two periods are shown in this figure).

The SCFT formulation finishes by adjusting the fields until equations (1-7) are satisfied. Once the self-consistency is achieved, the total free energy is evaluated as

$$\frac{F}{n_p k_B T} = -\ln\left(\frac{Q}{V}\right) + \frac{1}{V}\int d\mathbf{r}\chi N \phi_A(\mathbf{r})\phi_B(\mathbf{r}) - \frac{1}{V}\int d\mathbf{r}\Big(w_A(\mathbf{r})\phi_A(\mathbf{r}) + w_B(\mathbf{r})\phi_B(\mathbf{r})\Big) - \frac{1}{V}\int d\mathbf{r}\Big(2\eta_A(x,y)\phi_A(\mathbf{r}) + 2\eta_B(x,y)\phi_B(\mathbf{r})\Big)\delta(z) aN^{1/2}. \quad (8)$$

Throughout this report, χN and f are fixed to 20 and 0.3, respectively, which are typical parameter values for cylinder-forming diblock copolymers. In the bulk state, the naturally forming cylinder-to-cylinder distance is $L_0 = 1.69aN^{1/2}$, as shown in Figure 1(a). Repeating chemical patterns with period L_s is assumed in x direction, and H is the parameter for the film thickness in z direction, as shown in Figure 1(b). The substrate surface is set to consist of alternating 15% A-preferable stripe where $\eta_A = 0.6$ and 85% neutral area where $\eta_A = 0$. Although $\eta_i(x,y)$ can accommodate any two dimensional pattern, the stripe geometry treated in this work makes it only a function of x.

Our SCFT calculation is performed in a rectangular cell of

size $L_x \times L_y \times L_z$, with spatial lattice numbers of $100 \times 40 \times 30$, and the two-dimensional lattice of 100×40 at $z = 0$ is modeled as the stripe-patterned surface of the selective substrate. Neumann boundary conditions are imposed in two directions, y and z, to correctly represent polymer-polymer, polymer-air and polymer-substrate boundaries. The x direction is somewhat subtle because the resulting morphology sometimes does not have a proper reflecting symmetry in that direction as we see later. Thus, Neumann or periodic boundary condition is imposed depending on the symmetry of the morphologies we expect. In the direction of the chain contour length, 200 segments are used ($\Delta s = 0.005$). It is unusually high compared to other SCFT works, because the delta function potential imposed at $z = 0$ can be problematic at larger Δs. For the actual evaluation of the modified diffusion equation, we use a real space SCFT method improved by Yang *et al.*,[42] which is known to eliminate material conservation problem found in most real space methods.

3 Theoretical Results and Discussion

With this SCFT calculation, our primary objective is the creation of cylindrical microdomains vertically aligned with long-range order. We need to determine the optimal chemical pattern period L_s and film thickness H for the phase $1HnV$ (n=1,2,3,4), in which n columns of vertical cylinders are formed in between two horizontal hemicylinders sitting on the striped region. It is also important to investigate their competition with other morphologies which may break the long-range order of $1HnV$ patterns or be the source of defects. Thus, in the first stage, free energy per chain for each $1HnV$ phase is minimized over three spatial directions of the unit cell for the purpose of finding the optimal period of chemical pattern, which we denote as L_s^{1HnV}. In the second stage, in order to understand the stability of $1HnV$, we first identify all phases competing with $1HnV$ at the given $L_s = L_s^{1HnV}$. Then, the competition between phases are studied by comparing their free energies as a function of chemical pattern period L_s or film thickness H, now with free energy minimization over two spatial directions after fixing L_s or over only one spatial directions after fixing L_s and H. Note that such a thorough investigation is done representatively only for $1H2V$ and $1H3V$ morphologies.

3.1 Optimal conditions for $1HnV$

In films without any surface interaction, the equilibrium morphology of cylinder-forming BCPs is usually hexagonally-packed cylinders aligned vertically with respect to the substrates, and the cylinder-to-cylinder distance remains the same as the bulk case, L_0.[51,56] If the substrate becomes selective, horizontal cylinders may occur depending on the selectivity and film thickness, and the cylinder-to-cylinder distance will deviate from L_0 due to the geometrical constraint. In the current work where regional selectivity is considered, even though the final morphology can become quite complicated, it is still a generally acceptable rule that nature always tries to find a way to keep the cylinder-to-cylinder distance not too far from L_0, and the distance between cylindrical layers are similar to L_1 or L_2 given by Figure 1(a).

Since our goal is to suggest a strategy to control the long-range order of the vertical cylinder arrays of BCP microdomains on a sparse chemical pattern, first we show in Figure 2(a-h) the target morphologies of $1HnV$ phase (n=1,2,3 and 4) at the parameter set which minimizes the free energy for the given morphology. For these morphologies, on the A-preferable stripes, horizontal hemicylinders are always stuck to the stripe, while on the neutral region, given number and shape of vertical cylinder arrays are formed. This is in agreement with the experimental results,[40,44,47] and the case for $1H1V$ was intensely analyzed in the previous simulation.[42] As the most preferable period, we get $L_s^{1H1V} = 3.03aN^{1/2}$, $L_s^{1H2V} = 4.50aN^{1/2}$, $L_s^{1H3V} = 5.98aN^{1/2}$, $L_s^{1H4V} = 7.51aN^{1/2}$, as explained in the figure caption.

It is interesting that for each $1HnV$ phase, many similar morphologies are found which we may collectively call $1HnV$ family, and the difference between each member of the family is mainly the relative position of vertical cylinders across the horizontal hemicylinder. Depending on the vertical cylinder position, the bottom shapes of the horizontal hemicylinders also change. Here we only present the morphologies with minimum (*peristaltic*) and maximum (*undulatory*) free energies and they are labeled by postfixes "-p" and "-u", respectively. Note that all the morphologies in between "-p" and "-u" are allowed, and their free energy values lie in between the free energies of these two morphologies (for details, please refer to ref. 42 where only $1H1V$ was studied and A-preferable stripe covers 30% of the substrate). In order to visualize the exact morphology, examples of the bottom surface density profile for $1H3V$ phases are shown in Figure 2 (i) and (j). For each $1HnV$ phase shown in Figure 2, $1HnV$-p is energetically more favorable than $1HnV$-u. However, the free energy difference per chain is less than $3 \times 10^{-4} k_B T$, and thus it is possible that in real experiments, the coexistence of $1HnV$-p and $1HnV$-u may slightly break the long-range order across the hemicylinders. Since their free energies are nearly identical, we will use the data for $1HnV$-p in most discussions, as long as the distinction between the family members is not necessary.

In an effort to estimate the optimal pattern period for $1HnV$, we assume that it can be expressed as $L_s^{1HnV} = (n-1)\alpha + 2\beta$, where α is the spacing between columns of vertical cylinders and β is the spacing between the horizontal and vertical domains. From the periods of $1HnV$ presented in Figure 2, we roughly estimate that $\alpha \approx \beta \approx 1.5aN^{1/2}$, which is very close

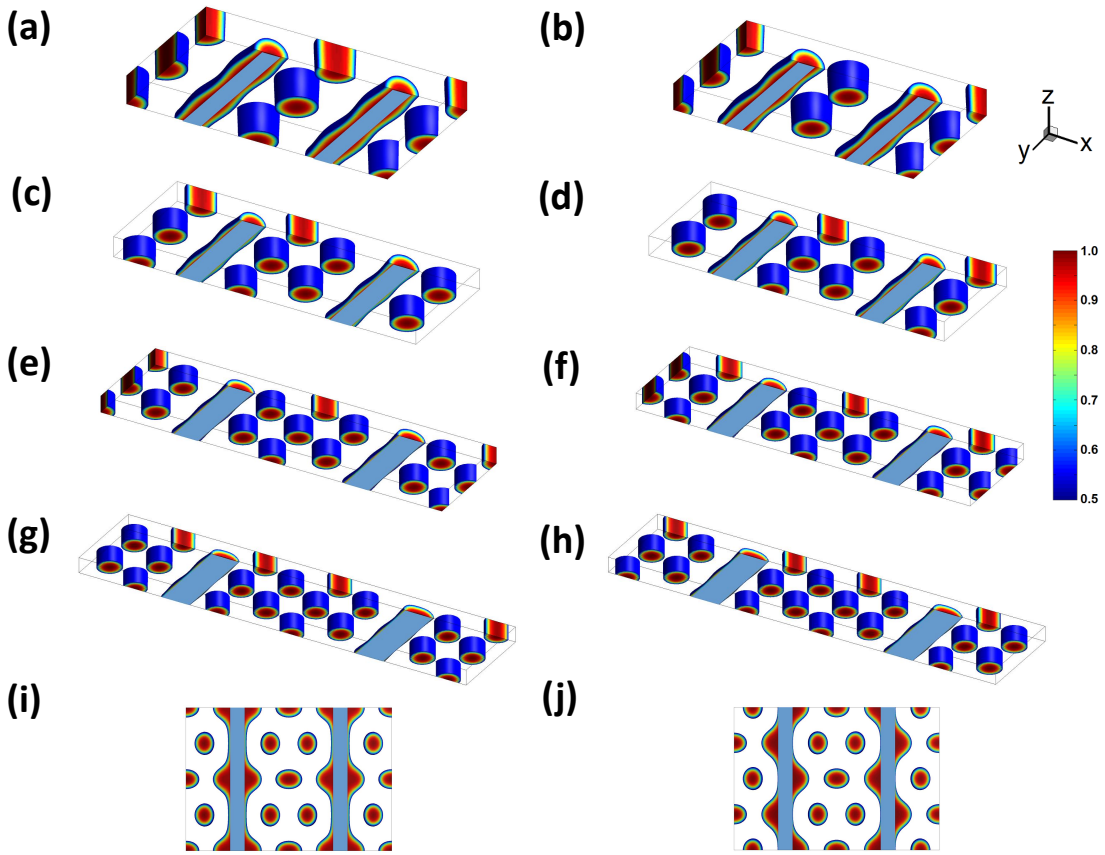

Fig. 2 $1HnV$ phases of cylinder-forming AB diblock copolymer ($\chi N = 20$ and $f = 0.3$) thin films in two pattern periods of the substrate shown in Figure 1(b): (a) $1H1V$-p in a cell of $6.06 \times 3.20 \times 0.66\ R_0^3$; (b) $1H1V$-u in a cell of $6.06 \times 3.20 \times 0.67\ R_0^3$; (c) $1H2V$-p in a cell of $9.00 \times 3.28 \times 0.59\ R_0^3$; (d) $1H2V$-u in a cell of the same size of (c); (e) $1H3V$-p in a cell of $11.96 \times 3.32 \times 0.57\ R_0^3$; (f) $1H3V$-u in a cell of the same size of (e); (g) $1H4V$-p in a cell of $15.02 \times 3.32 \times 0.58\ R_0^3$; (h) $1H4V$-u in a cell of the same size of (g). The color bars correspond to the density of A block domain. The free energy for each morphology is minimized over x (the period of chemical pattern L_s), y and z (film thickness H) directions. (i) and (j) are the density profile at the bottom surface of (e) and (f) but with a larger cell size, respectively, for better illustrating the bottom shape of hemicylinders ((i) for *peristaltic* and (j) for *undulatory*).

to $\sqrt{3}L_0/2 = 1.46aN^{1/2}$. It is quite obvious that α is essentially the layer-to-layer spacing L_1 shown in Figure 1(a). This is also in agreement with the experimental result of Park *et al.*.[44] In Rasmussen's SCFT calculation for DSA of cylinder-forming BCPs confined in a neutral groove, if the groove width was integer times of L_1, vertical cylinders formed on a regular hexagonal lattice and α assumed exact the same value of L_1.[28] In our case that BCPs self-assemble on a sparse chemical pattern, α is a little bit larger than L_1, because it is slightly modified due to the crossed-cylinder morphology. As for β being equal to α, it is partially a coincidence due to the size of the selective part of the substrate.

The chemical pattern period is a tunable parameter in real experiments. For the purpose of systematically investigating the effects of its mismatch, we calculate the free energy of each $1HnV$ phase as a function of L_s, and the results are shown in Figure 3(a). Focusing on the stable phases with minimum free energies, it can be seen that the number of vertical cylinder layers, n, gradually increases with L_s, and each $1HnV$ is stable within a certain range of L_s.[28,29] When the chemical pattern period deviates from the optimal value for $1HnV$, $L_s^{1HnV} \approx 1.5(n+1)aN^{1/2}$, the free energy per chain increases. If we compare the relative deviation from the minimum free energy, the penalty decreases as we move from $1H1V$ to $1H4V$, as shown in Figure 3(b). Obviously, the deviation of L_s from the optimal values results mainly in excessive stretch or compression of copolymer domains, which is distributed on all the cylindrical columns; thus at the same absolute deviation from L_s^{1HnV}, the free energy increase becomes less severe at larger n. It also gives a warning that even near the optimal period, L_s^{1HnV}, the free energy difference between $1HnV$ phase and the competing one, $1H(n-1)V$ or $1H(n+1)V$, may not be large enough to suppress the wrong morphology. In conclusion, more defects may sneak in as n increases, and other experimental techniques to enhance long-range order may be required.

For morphologies given in Figure 2, we have known that $\alpha \approx \beta \approx 1.5aN^{1/2}$; while for different L_s in Figure 3, $\alpha \approx \beta$ remains valid but their values change approximately linearly with L_s, which agrees with Rasmussen's calculation in spite of the difference that in our system BCPs are confined by hemicylinders formed on chemical patterns instead of nanowalls forming grooves.[28] Thus it may be possible in experiments to obtain $1HnV$ arrays with desired α and β by tuning the chemical pattern period, L_s, under the condition that L_s should not deviate too much from its optimal value for $1HnV$, and defects originated from competing phases must be considered as we will discuss later.

In order to understand the competition between phases with peristaltic and undulatory hemicylinders, in Figure 3(c) we present the free energy difference between $1HnV$-p and $1HnV$-u phases as a function of the reduced chemical pattern

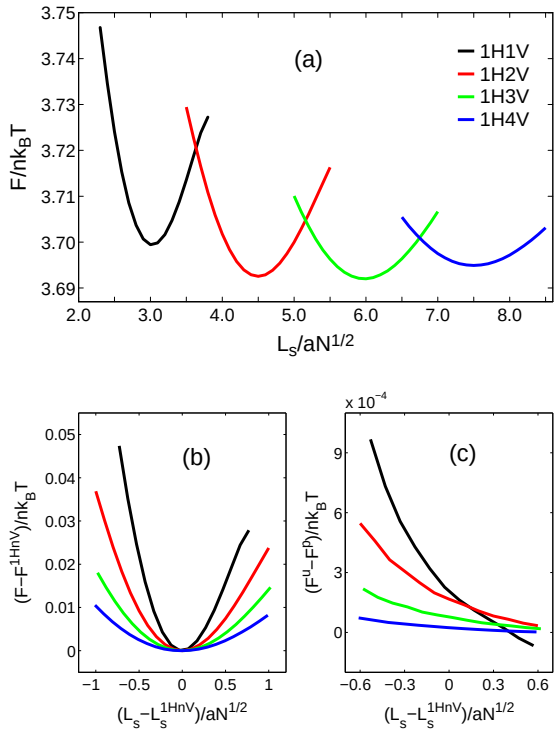

Fig. 3 (a) Free energy comparison for $1HnV$ (n=1,2,3 and 4) phases as a function of chemical pattern period L_s. (b) The reduced free energies $F - F^{1HnV}$ as a function of reduced chemical pattern period $L_s - L_s^{1HnV}$, where F^{1HnV} is the free energy corresponding to morphologies shown in Figure 2 (a), (c), (e) and (g). (c) The free energy difference between $1HnV$ phases with peristaltic(F^p) and undulatory(F^u) hemicylinders at the bottom surface, plotted as a function of reduced chemical pattern period $L_s - L_s^{1HnV}$.

period, $L_s - L_s^{1HnV}$. It can be seen that the free energy for $1HnV$-p is usually lower, though the difference decreases for increasing n. It is natural to think that the stretch or compression sharing mechanism for Figure 3(b) is also valid for this case. It is interesting that for L_s around L_s^{1HnV} where $1HnV$ is most stable, the difference decreases as L_s increases and $1HnV$-u may become favorable at large enough L_s, especially for $1H1V$. This observation suggests that using L_s slightly smaller than L_s^{1HnV} may be helpful in removing $1HnV$-u when creating wide area of $1HnV$ morphology, though it is not certain that the small free energy difference is enough to distinguish them in real experiments.

3.2 Stability of $1H2V$ and $1H3V$

So far, we have tested the competition between $1HnV$ phases (n =1, 2, 3 and 4), and it is found that $1HnV$ is stable within a certain range around $L_s^{1HnV} \approx 1.5(n+1)aN^{1/2}$. However, even within that specific range, some other morphologies may compete and break the long-range order of $1HnV$ morphology. Due to factors such as substrate irregularity and incomplete annealing, the fabricated film may not reach to the complete equilibrium, and the thickness fluctuation may widely exist in the final morphology.[57] It is also noteworthy that for some copolymer films the final morphology may strongly depend on the initial thickness of the film,[58] especially when there are metastable states that the system can be trapped in. An example is Yang *et al.*'s SCFT[42] calculation which provided a good explanation to the existence of defects in Kim *et al.*'s experiment.[40] By investigating the role of film thickness in a relatively larger range, the stability of $1H1V$ phase was well understood and an unstable phase was also identified which was capable of thinning the films and consequently providing instability for the ordering of the thicker film nanostructures.

In this subsection, we investigate phases competing with $1HnV$ at the given optimal period, L_s^{1HnV}. For the case of $1H2V$, with L_s near $L_s^{1H2V} = 4.50aN^{1/2}$, mainly three competing morphologies are found. Among them, $1H2zV$-p and $1H2zV$-u are shown in Figure 4 (a) and (b). Although there are essentially 4 columns of vertical cylinders in one chemical pattern period, it is a subtle issue to give them proper names. In $1H4V$ phases, 4 columns of vertical cylinders are clearely seen in one chemical pattern period, while in $1H2zV$ family those vertical cyliners are seemingly arranged in two zigzag shaped columns. In a quantitative description, for $1H4V$ family, the spacing between cylinders in y direction is close to L_0 and the spacing between columns of vertical cylinders in x direction is close to L_1. Now if $1H2zV$ phases are measured in the same way, the corresponding values are very close to $2L_1$ and L_2, respectively. At a glance, such geometric relations may seem difficult to understand, but they can be easily explained by the left and right illustrations of Figure 1(a).

In other words, the arrangement of vertical cylinders in both $1H4V$ and $1H2zV$ phases can be regarded as part of the bulk array, but their directions are tilted by 30° as explained in Figure 1(a). With L_s near L_s^{1H2V}, $1H2zV$ is unfavorable compared with $1H2V$ due to the relatively larger excessive compression and stretching energy. There are many signs indicating the required sacrifice of making $1H2zV$ phase. For $1H2V$ phase, there are vertical cylinders with center-to-center distance of L_0, while for $1H2zV$ phase, the distance is $2L_1 = \sqrt{3}L_0$. As a consequence of this geometry, the distance between the crossed-cylinders vary much more for $1H2zV$ phase, and the cross sections of vertical cylinders distant from the horizontal hemicylinder deform heavily from circle to ellipse, as highlighted in Figure 4 (a) and (c). Also, the positions of vertical cylinders in $1H2zV$ are strongly distorted in a way that one's eye usually count 2 zigzag columns instead of 4 linear columns. For this reason and also considering that they compete with $1H2V$ phases, we call them $1H2zV$ phases, where "zV" is an abbreviation for the words "zigzag vertical".

In addition to $1H2zV$ phases, there exists another competing phase, $3H$, as shown in Figure 4(e). The name nH is given for a phase with only n horizontal hemicylinders in one period. An even n would make a natural morphology resembling the bulk one, with film thickness close to L_2. However, with L_s near L_s^{1H2V}, no such phases can fit in one period, and $3H$, a phase with one hemicylinder on the selective region and two hemicylinders on the upper surface, turns out to make a competition. For this phase, the minimum free energy is found at $H = 0.75aN^{1/2}$; *i.e.* the film is slightly thinner than the simple estimation, $L_2 = 0.85aN^{1/2}$. It is noteworthy that this thickness is still significantly larger than the equilibrium thickness for $1H2V$ phase, $H = 0.59aN^{1/2}$. This can not be easily understood by comparing $3H$ to part of the bulk array.

Since chemical pattern period is a tunable parameter in experiment, we have performed systematical investigation of the effect of L_s on all these competing morphologies, and the results are displayed in Figure 5(a). As discussed above, all the phases other than $1H2V$ have some flaws which result in free energy increase, and thus $1H2V$ is always the stable phase. The free energy of $1H2zV$ is always higher than that of $1H2V$, but the difference decreases at large L_s, and this trend is more remarkable for $1H2zV$-u than $1H2zV$-p; *i.e.* phases with undulatory horizontal hemicylinders may have a lower free energy than those with peristaltic horizontal hemicylinders at large enough L_s, as explained in Figure 3(c) for the case of $1H2V$.

Discussions so far suggest that change of L_s around L_s^{1H2V} does not have large influence enough to change the equilibrium morphology, as long as the film thickness can adjust to find the minimum free energy. However, if we consider the situation that the film thickness H is externally given, the competition becomes more interesting. In Figure 5(b), we present the

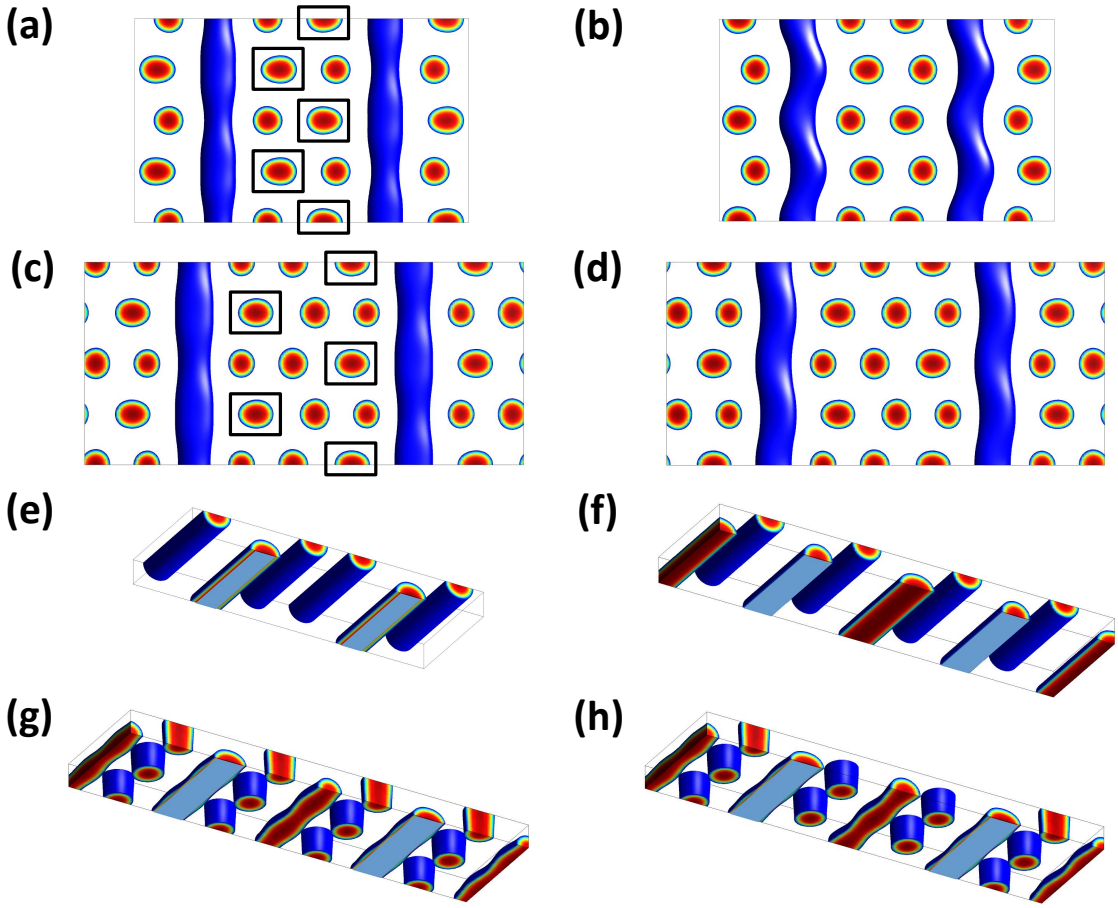

Fig. 4 Phases competing with $1H2V$ or $1H3V$: (a) $1H2zV$-p in a cell of $9.00 \times 6.28 \times 0.59\ R_0^3$ (some cross sections of ellipse shape are hightlighted with frames); (b) $1H2zV$-u in a cell of $9.00 \times 6.24 \times 0.59\ R_0^3$; (c) $1H3zV$-p in a cell of $11.96 \times 6.12 \times 0.57\ R_0^3$ (some cross sections of ellipse shape are hightlighted with frames); (d) $1H3zV$-u in a cell of the same size as (c); (e) $3H$ in a cell of $9.00 \times 3.28 \times 0.75\ R_0^3$; (f) $4H$ in a cell of $11.96 \times 3.32 \times 0.78\ R_0^3$; (g) $2H2V$-p in a cell of $11.96 \times 3.24 \times 0.69\ R_0^3$; (h) $2H2V$-u in a cell of the same size as (c). The free energy for each morphology is minimized over y and z (film thickness H) directions at the given optimal chemical pattern period L_s.

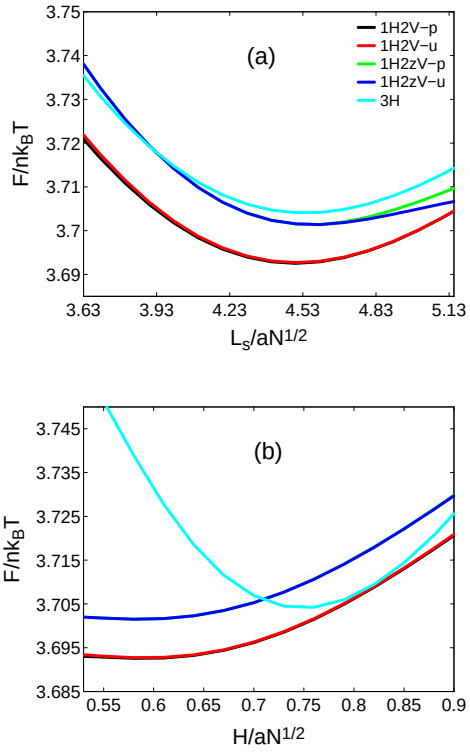

Fig. 5 Free energy comparison of $1H2V$ with the competing phases. (a) Free energy F vs. pattern period L_s, where the free energy is minimized over y and z directions. (b) Free energy F vs. film thickness H, where L_s is fixed as L_s^{1H2V} and the free energy is minimized over only y direction. Note that in this figure each phase family has nearly identical free energy.

free energies of competing phases as a function of H with fixed $L_s = L_s^{1H2V}$. At all film thicknesses we consider, $1H2V$ phase is still with the lowest free energy, and $1H2zV$ phase is comfortably above it. However, depending on the thickness, $3H$ phase can have nearly the same free energy as $1H2V$ phase. The closest approach happens at around $L_s = 0.82aN^{1/2}$, and we expect that if the block copolymer film has some thickness undulation, defects locally resembling the shapes of $3H$ morphology may be difficult to remove.

The above story is repeated to a degree for the case of $1H3V$ morphology. It is found that there exist competing phases of $1H3zV$-p and $1H3zV$-u as shown in Figure 4 (c) and (d) in which the vertical cylinders are aligned according to the right illustration of Figure 1(a). The vertical cylinder shapes and positions are strongly distorted in a way that a pair of vertical cylinder columns may be counted as one staggered vertical column, so that we end up counting 3 zigzag columns.

Even though the main idea remains the same, the situation is more complicated compared to the $1H2V$ case. Due to the relatively large pattern period, $L_s^{1H3V} = 5.98aN^{1/2}$, many phases are found to compete with the $1H3V$ phase and we only present 5 representative ones here. Two of them, $1H3zV$-p and $1H3zV$-u, are explained above and another one, $4H$ phase, which is entirely composed of horizontal hemicylinders is displayed in Figure 4(f). Because 4 is an even number, this morphology resembles the bulk one, and its equilibrium film thickness $0.78aN^{1/2}$ is close to $L_2 = 0.85aN^{1/2}$. The other two phases are what we call $2H2V$-p and $2H2V$-u and they are shown in Figure 4 (g) and (h), respectively. They can be regarded as $1H1V$ phase repeating twice in one L_s period. One can imagine a few different combinations of peristaltic and undulatory horizontal hemicylinders for the two different hemicylinder positions, and it is even possible that the hemicylinders on the neutral region may migrate to the top surface. All of them turn out to have similar free energies, and we only present two representative ones, $2H2V$-p and $2H2V$-u phases.

As we did for $1H2V$, we have calculated the free energy for each phase competing with the $1H3V$ phase as a function of chemical pattern period L_s in Figure 6(a). We again confirm that $1H3V$ is always the stable phase, though free energy for $4H$ phase comes within $0.01k_BT$. Also, as we observed for the case of $1H2V$, the free energy difference between $1H3V$ phase and $1H3zV$ phases reduces below $0.005k_BT$ at large L_s, which can be a significant obstacle in maintaining the long-range order of $1H3V$ phase.

Their free energy comparison as a function of film thickness H is shown in Figure 6(b). It turns out that the effect of film thickness fluctuation is much more remarkable in this case. From Figure 6(b), it can be seen that as the thickness increases, the free energy gap with other phases reduces. Moreover, if $H > 0.75aN^{1/2}$, $4H$ phase can have lower energy than $1H3V$ phase, and we expect that a film with $4H$ morphology may be

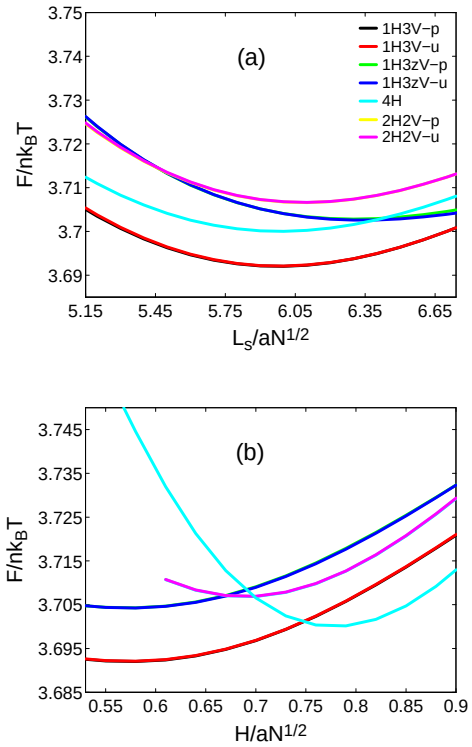

Fig. 6 Free energy comparison of $1H3V$ with the competing phases. (a) Free energy F vs. pattern period L_s, where the free energy is minimized over y and z directions. (b) Free energy F vs. film thickness H, where L_s is fixed as L_s^{1H3V} and the free energy is minimized over only y direction. $2H2V$ phases fail to survive at small enough film thickness, so the corresponding curves are not complete. Note that in this figure each phase family has nearly identical free energy.

trapped in a metastable state and it may take a long time for the film to find a dynamic route to reduce the thickness and find the $1H3V$ phase. With a simple geometric consideration, we expect that $1HnV$ morphology with odd n must compete with the naturally ordered $(n+1)H$ phase with even $n+1$, and it is desirable to avoid such a competition; *i.e.* one possible strategy is to design nanomaterials having $1HnV$ phase with even n only. More important than choosing an even n, as can be concluded from both Figure 5(b) and 6(b), the film should be thin enough in case it is trapped in undesirable metastable morphologies. For example, if $1H2V$ phase is desired, only a film thickness of $H < L_0/2$ is appropriate.

4 Experimental Results and Discussion

We carried out directed self-assembly experiment based on poly(styrene-*block*-methyl methacrylate) (PS-*b*-PMMA) with a parameter set fitting for $1H2V$ structure. Hydroxyl-terminated poly(styrene-*random*-methyl methacrylate) (PS-r-PMMA) was synthesized by living free-radical polymerization. Anhydrous toulene was purchased from Aldrich. Hydroxyl-terminated PS-r-PMMA was deposited on the oxidized Si substrate by spin coating of 1 wt% toulene solution. The brush polymer coated substrate was annealed in vacuum oven at 160 °C for a day after unreacted polymers were washed out with toluene. In order to make a chemical pattern, a disposable photoresist pattern (shinEtsu) was prepared on the monolayer brush of PS-*r*-PMMA by ArF lithography. The photoresist pattern had a 1:1 line-and-space ratio with a 145 nm of period (L_s), *i.e.*, the original photoresist pattern was a symmetric one with space width of 72.5 nm. Then thermal treatment was applied to form asymmetric photoresist pattern at 150 °C for 40 seconds. The photoresist pattern width was therefore increased by thermal flow process and space was shrunken to 35 nm. After oxygen reactive ion etching (RIE), asymmetric chemical patterns of oxidized brush were obtained, where the 35 nm wide oxidized lines of chemical pattern became the sites which prefer PMMA domains. Residual photoresist pattern was completely removed by sonication in toluene.

For the purpose of creating well ordered $1H2V$ structure, a cylinder-forming diblock copolymer film of PS-*b*-PMMA was spin-coated on the prepatterned substrate consisting of oxidized sparse stripes, then it is annealed at 200 °C in a vacuum oven for a day. For the fine tuning of block copolymer period, we used a mixture of two different block copolymers, (i) 46,000-21,000 (PDI = 1.09) and (ii) 140,000-60,000 (PDI = 1.16) of molecular weight from Polymer Source Inc.. The PMMA cylinder-to-cylinder distance can be tuned by controlling the mixture ratio. In our sample, we used 1:1 mixture ratio, which produced cylindrical arrays with cylinder-to-cylinder distance of approximately 48 nm. The film thickness

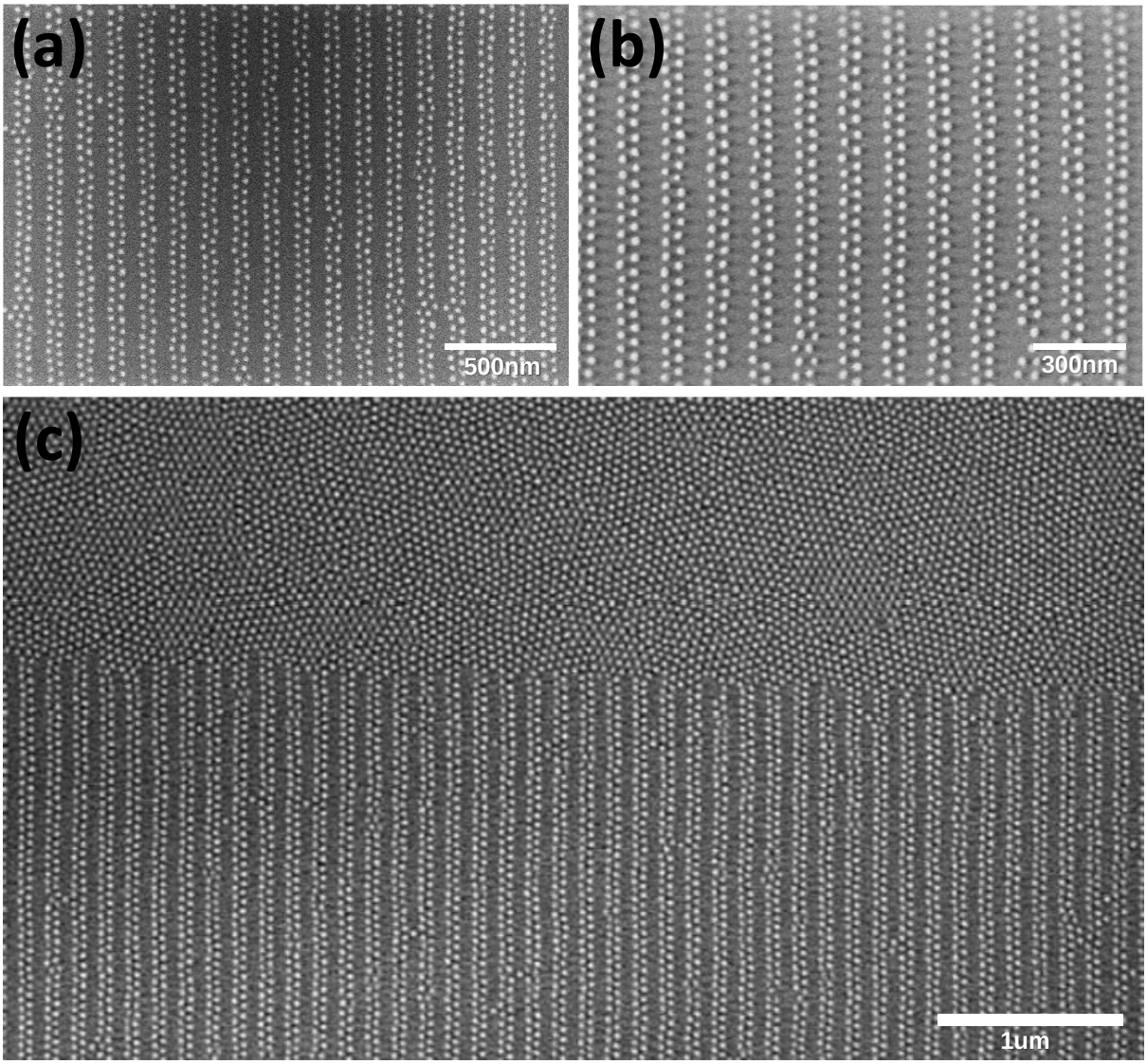

Fig. 7 SEM images of 1*H*2*V* morphology, based on the self-assembly of PS-*b*-PMMA block copolymers on a neutral substrate with stripe-shaped oxidized prepattern. (a) An SEM image of Al nanodots created by pattern transfer. The vertically aligned cylinders were replicated to Si wafer by selective PMMA etching and aluminum deposition followed. (c) Wide-range SEM image of Al nanodots created on non-patterned region (upper part) and patterned region (lower part).

was measured to be approximately 20 nm, which fulfills the requirement deduced from our theoretical calculations.

In the final step, the vertically aligned cylinders were replicated to Si wafer by selective PMMA etching and aluminum deposition. In order to etch PMMA cylinders selectively, UV cross-linkers were first used for the degradation of PMMA, and O_2 RIE was used for the complete etching of PMMA.[59] After all the treatment, Aluminum nanodots with 10 nm of height were obtained by thermal evaporation in vacuum chamber, and residual polymer templates were removed by sonication in toluene.

In order to confirm the final morphology, SEM images were obtained by Hitachi S-4800 and the result shows that highly ordered aluminum nanodots with $1H2V$ structure are formed on the Si surface (see Figure 7(a)). The stripe shaped region unoccupied by Al nanodots indicates the original position of the horizontal PMMA hemicylinders which were formed on the oxidized region. It is clear that the position and orientation of PMMA domains were controlled as we demonstrated in the simulation. Figure 7(b) is an enlarged SEM image, and we can see that the created Al nanodots have uniform size distribution. Even though their long-range order is excellent, the $1H2V$-p and $1H2V$-u phases are not easily distinguishable in the SEM image and their coexistence seem to be inevitable as expected in our simulation results. Also, there are finite numbers of vacancy and interstitial defects. Even though we did not track their origin, the cylindrical shapes of interstitial defects suggest that the defects are originated from the block copolymer domains.

Figure 7(c) shows the wide-range SEM image of aluminum dots array with and without the prepattern. The metal nanodots are hexagonally ordered in the upper part of the image where photoresist pattern is not present. However, the hexagonal array is far from being perfect. There are many grain boundaries and the long-range order is completely lost in a few hundred nm scale. On the other hand, highly regulated arrays of metal nanodots with long-range order have been accomplished over micrometer length scale as shown in the lower part of the SEM image.

5 Conclusions

By combining SCFT calculation and experiment, we have studied the directed self-assembly of cylinder-forming diblock copolymer thin films deposited on sparsely patterned substrates, and a systematic analysis has been made to achieve a fundamental understanding of creating perfectly ordered block copolymer nanostructures at various chemical pattern period of the substrate, L_s. With SCFT simulation, we first explored the three-dimensional parameter space and determined the optimal conditions for the targeted crossed-cyliner morphologies which we call $1HnV$ (n =1, 2, 3 and 4) phases. For each $1HnV$ family, it was found that the optimal value of L_s is around $1.5(n+1)aN^{1/2}$, and a pair phases with peristaltic or undulatory horizontal hemicyliners were also identified. Within each $1HnV$ family, at optimal pattern period L_s^{1HnV}, the phase with peristaltic hemicylinders always has a lower free energy than the one with undulatory hemicylinders, though the difference may be not large enough to be distinguished in real experiments.

Furthermore, many phases competing with $1H2V$ and $1H3V$ phases were identified near their respective optimal value of L_s, three for $1H2V$ and five for $1H3V$. By comparing their free energies, we found that $1H2V$ and $1H3V$ are stable morphologies for a wide range of L_s values provided that the thickness fluctuation is minimized. However, in a situation with strong thickness fluctuation, phases with only horizontal hemicylinders may compete strongly, and defects resulting from such phases may break the long-range order of the final morphology of the thin film. One possible strategy we found to suppress such defects is to design nanomaterials having $1HnV$ phase with even n only.

Finally, as a sample system, almost perfectly aligned $1H2V$ morphology composed of PS-*b*-PMMA diblock copolymers on stripe-shaped oxidized prepattern was created. By selective PMMA etching and aluminum deposition, the nanostructure is transferred to create highly-ordered Al nonodot arrays. Our results demonstrate that directed self-assembly of block copolymers on sparse chemical pattern is a promising pathway to high-density nanostructures, and useful insight for enhancing their long-range order is also provided.

6 Acknowledgements

This research was supported by Basic Science Research Program through the National Research Foundation of Korea (NRF) funded by the Ministry of Education, Science and Technology (2012R1A1A2043633 and 2014R1A2A1A11054430). Y. J. Choi and S. O. Kim were financially supported by the Institute for Basic Science (IBS). PLSI supercomputing resource of KISTI is also appreciated.

References

1 J. Y. Cheng, C. A. Ross, V. Z.-H. Chan, E. L. Thomas, R. G. H. Lammertink and G. J. Vancso, *Adv. Mater.*, 2001, **13**, 1174–1178.
2 R. A. Segalman, *Mater. Sci. Eng. R*, 2005, **48**, 191–226.
3 C. J. Hawker and T. P. Russell, *MRS Bull.*, 2005, **30**, 952–965.
4 J. Bang, U. Jeong, D. Y. Ryu, T. P. Russell and C. J. Hawker, *Adv. Mater.*, 2009, **21**, 4769–4792.
5 I. W. Hamley, *Prog. Poly. Sci.*, 2009, **34**, 1161–1210.

6 D. O. Shin, J. H. Mun, G.-T. Hwang, J. M. Yoon, J. Y. Kim, J. M. Yun, Y.-B. Yang, Y. Oh, J. Y. Lee, J. Shin, K. J. Lee, S. Park, J. U. Kim and S. O. Kim, *ACS NANO*, 2013, **7**, 8899–8907.

7 H.-C. Kim, S.-M. Park and W. D. Hinsberg, *Chem. Rev.*, 2010, **110**, 146–177.

8 C. G. Hardy and C. Tang, *J. Polym. Sci.: Part B: Polym. Phys.*, 2013, **51**, 2–15.

9 A. Matsushita and S. Okamoto, *Macromolecules*, 2014, **47**, 7169-7177.

10 M. Bockstaller, R. Kolb and E. L. Thomas, *Adv. Mater.*, 2001, **13**, 1783–1786.

11 A. C. Edrington, A. M. Urbas, P. DeRege, C. X. Chen, T. M. Swager, N. Hadjichristidis, M. Xenidou, L. J. Fetters, J. D. Joannopoulos, Y. Fink and E. L. Thomas, *Adv. Mater.*, 2001, **13**, 421-425.

12 K. Koo, H. Ahn, S.-W. Kim, D. Y. Ryu and T. P. Russell, *Soft Matter*, 2013, **9**, 9059–9071.

13 C. Tang, A. Tracz, M. Kruk, R. Zhang, D.-M. Smilgies, K. Matyjaszewski and T. Kowalewski *J. Am. Chem. Soc.*, 2005, **127**, 6918–6919.

14 H.-C. Kim and W. D. Hinsberg, *J. Vac. Sci. Technol. A*, 2008, **26**, 1369–1382.

15 M. Takenaka, S. Aburaya, S. Akasaka, H. Hasegawa, N. Hadjichristidis, G. Sakellariou, Y. Tada and H. Yoshida, *J. Polym. Sci.: Part B: Polym. Phys.*, 2010, **41**, 2297–2301.

16 B. H. Kim, S. J. Park, H. M. Jin, J. Y. Kim, S.-W. Son, M.-H. Kim, C. M. Koo, J. Shin, J. U. Kim and S. O. Kim, *Nano Lett.*, 2015, **15**, 1190–1196.

17 F. S. Bates and G. H. Fredrickson, *Physics Today*, 1999, **52**, 32–38.

18 T. L. Morkved, M. Lu, A. M. Urbas, E. E. Ehrichs, H. M. Jaeger, P. Mansky and T. P. Russell, *Science*, 1996, **273** 931-933.

19 M. W. Matsen, *Phys. Rev. Lett.*, 2005, **95**, 258302–4.

20 D. E. Angelescu, J. H. Waller, D. H. Adamson, P. Deshpande, S. Y. Chou, R. A. Register and P. M. Chaikin, *Adv. Mater.*, 2004, **16**, 1736–1740.

21 J. Bodycomb, Y. Funaki, K. Kimishima and T. Hashimoto, *Macromolecules*, 1999, **32**, 2075-2077.

22 J. W. Jeong, W. I. Park, M.-J. Kim, C. A. Ross and Y. S. Jung, *Nano Lett.*, 2011, **11**, 4095-4101.

23 M. Kimura, M. J. Misner, T. Xu, S. H. Kim and T. P. Russell, *Langmuir*, 2003, **19**, 9910–9913.

24 S. H. Kim, M. J. Misner, T. Xu, M. Kimura and T. P. Russell, *Adv. Mater.*, 2004, **16**, 226–231.

25 D. Sundrani, S. B. Darling and S. J. Sibener, *Nano Lett.*, 2004, **4**, 273–276.

26 J. Y. Cheng, C. A. Ross, H. I. Smith and E. L. Thomas, *Adv. Mater.*, 2006, **18**, 2505–2521.

27 I. Bita, J. K. W. Yang, Y. S. Jung, C. A. Ross, E. L. Thomas and K. K. Berggren, *Science*, 2008, **321**, 939–943.

28 K. Ø. Rasmussen, *J. Polym. Sci.: Part B: Polym. Phys.*, 2004, **42**, 3695–3700.

29 S. Xiao, X. Yang, E. W. Edwards, Y.-H. La and P. F. Nealey, *Nanotechnology*, 2005, **16**, S324–S329.

30 Q.-y. Tang and Y.-q. Ma, *Soft Matter* 2010, **6**, 4460–4465.

31 S.-J. Jeong, H.-S. Moon, J. Shin, B. H. Kim, D. O. Shin, J. Y. Kim, Y.-H. Lee, J. U. Kim and S. O. Kim, *Nano Lett.*, 2010, **10**, 3500–3505.

32 S. Kim, D. O. Shin, D.-G. Choi, J.-R. Jeong, J. H. Mun, Y.-B. Yang, J. U. Kim, S. O. Kim and J.-H. Jeong, *Small*, 2012, **10**, 1563-1569.

33 A. Tavakkoli K. G., K. W. Gotrik, A. F. Hannon, A. Alexander-Katz, C. A. Ross and K. K. Berggren, *Science*, 2012, **336**, 1294-1298.

34 L. Rockford, Y. Liu, P. Mansky, T. P. Russell, M. Yoon and S. G. J. Mochrie, *Phys. Rev. Lett.*, 1999, **82**, 2602–2605.

35 X. M. Yang, R. D. Peters, P. F. Nealey, H. H. Solak and F. Cerrina, *Macromolecules*, 2000, **33**, 9575–9582.

36 S. O. Kim, H. H. Solak, M. P. Stoykovich, N. J. Ferrier, J. J. de Pablo and P. F. Nealey, *Nature*, 2003, **424**, 411–414.

37 E. W. Edwards, M. F. Montague, H. H. Solak, C. J. Hawker and P. F. Nealey, *Adv. Mater.*, 2004, **16**, 1315–1319.

38 M. P. Stoykovich, M. Müller, S. O. Kim, H. H. Solak, E. W. Edwards, J. J. de Pablo and P. F. Nealey, *Science*, 2005, **308**, 1442–1446.

39 S.-M. Park, G. S. W. Craig, Y.-H. La, H. H. Solak and P. F. Nealey, *Macromolecules*, 2007, **40**, 5084–5094.

40 S. O. Kim, B. H. Kim, D. Meng, D. O. Shin, C. M. Koo, H. H. Solak and Q. Wang, *Adv. Mater.*, 2007, **19**, 3271–3275.

41 Y.-B. Yang, Y. M. Jeon, J. U. Kim and J. Cho, *Eur. Phys. J. E*, 2012, **35**, 86.

42 Y.-B. Yang, S. J. Park, P. Kim and J. U. Kim, *Soft Matter*, 2013, **9**, 5624–5633.

43 J. Y. Cheng, C. T. Rettner, D. P. Sanders, H.-C. Kim and W. D. Hinsberg, *Adv. Mater.*, 2008, **20**, 3155–3158.

44 S. H. Park, D. O. Shin, B. H. Kim, D. K. Yoon, K. Kim, S. Y. Lee, S.-H. Oh, S.-W. Choi, S. C. Jeon and S. O. Kim, *Soft Matter*, 2010, **6**, 120–125.

45 R. Ruiz, H. Kang, F. A. Detcheverry, E. Dobisz, D. S. Kercher, T. R. Albrecht, J. J. de Pablo and P. F. Nealey, *Science*, 2008, **321**, 936–939.

46 Y. Tada, S. Akasaka, H. Yoshida, H. Hasegawa, E. Dobisz, D. Kercher and M. Takenaka, *Macromolecules*, 2008, **41**, 9267–9276.

47 J. Xu, S. Park, S. Wang, T. P. Russell, B. M. Ocko and A. Checco, *Adv. Mater.*, 2010, **22**, 2268–2272.

48 Y. A. Kriksin, P. G. Khalatur, I. V. Neratova, A. R. Khokhlov and L. A. Tsarkova, *Phys. Chem. C*, 2011, **115**,

25185–25200.
49 P. Chen, H. Liang, R. Xia, J. Qian and X. Feng, *Macromolecules*, 2013, **46**, 922-926.
50 F. A. Detcheverry, D. Q. Pike, P. F. Nealey, M. Müller and J. J. de Pablo, *Faraday Discuss.*, 2010, **114**, 111–125.
51 M. W. Matsen, *J. Phys.: Condens. Matter*, 2002, **14**, R21–R47.
52 G. H. Fredrickson, *The Equilibrium Theory of Inhomogeneous Polymers*, Oxford University Press: New York, USA, 2006.
53 J. U. Kim and M. W. Matsen, *Macromolecules*, 2008, **41**, 246–252.
54 J. U. Kim and M. W. Matsen, *Phys. Rev. Lett.*, 2009, **102**, 078303–4.
55 J. U. Kim and M. W. Matsen, *Soft Matter*, 2009, **5**, 2889–2995.
56 T. Thurn-Albrecht, R. Steiner, J. DeRouchey, C. M. Stafford, E. Huang, M. Bal, M. Tuominen, C. J. Hawker and T. P. Russell, *Adv. Mater.*, 2000, **12**, 787–791.
57 T. L. Morkved and H. M. Jaeger, *Eurphys. Lett.*, 1997, **40**, 643–648.
58 R. Limary and P. F. Green, *Macromolecules*, 1999, **32**, 8167–8172.
59 H.-S. Moon, D. O. Shin, B. H. Kim, H. M. Jin, S. Lee, M. G. Lee and S. O. Kim, *J. Mater. Chem.*, 2012, **22**, 6307–6310.

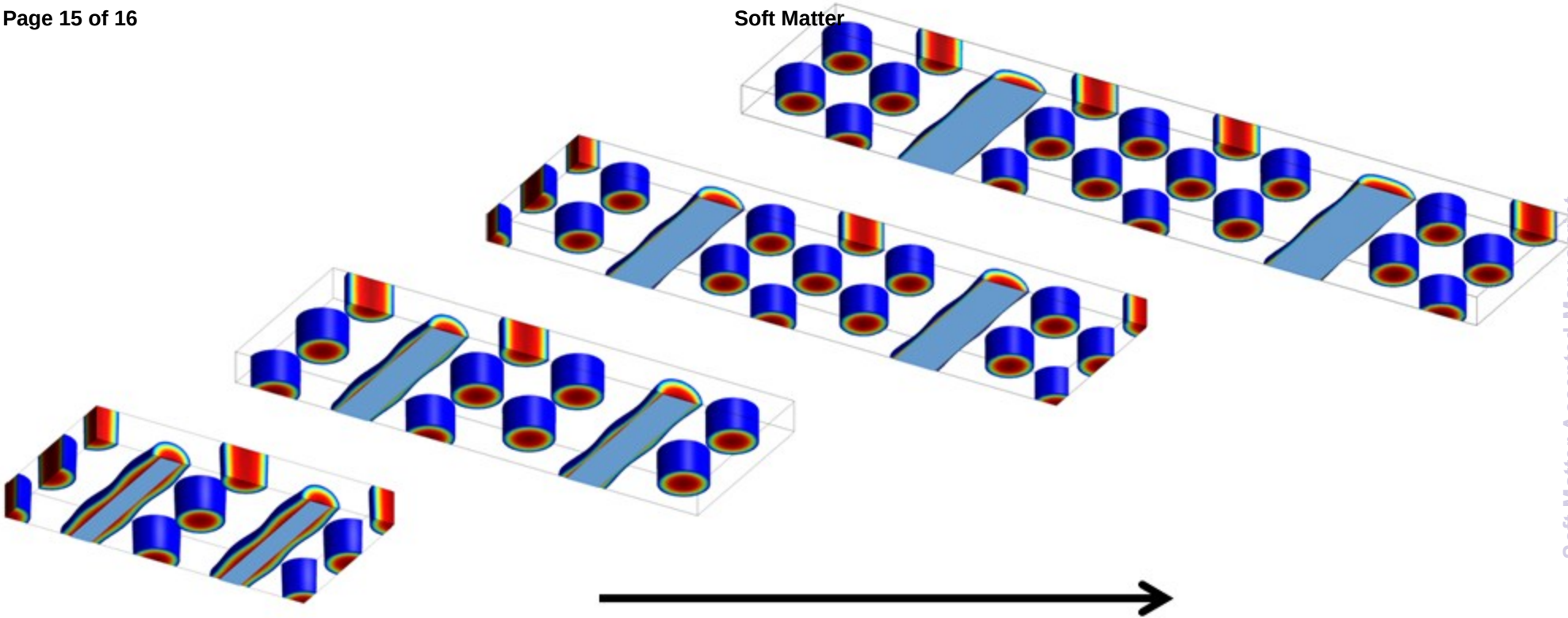

Pattern multiplication and directed self-assembly of block copolymer films deposited
on sparsely patterned substrates.